Novel Nano-Core–Shell Structure SiO$_2$@Ni-Reinforced Ni-P-Based Amorphous Composite Coating

ZHIHAO ZHAO,[1] SHUAI WANG,[1] MENG CHENG,[1] HAO JIANG,[1] SHUANGQING SUN,[1] CHUNLING LI,[1] and SONGQING HU[1,2]

1.—College of Materials Science and Engineering, China University of Petroleum (East China), Qingdao 266580, China. 2.—e-mail: songqinghu@upc.edu.cn

A Ni-P nanocomposite coating is one of the most widely applied corrosion- and wear-resistant coatings. However, the agglomeration of nanoparticles will reduce their performance. In this study, SiO$_2$@Ni nanoparticles with a core–shell structure were first prepared by pre-plating, and then SiO$_2$@Ni nanoparticles were introduced into Ni-P coating to achieve a Ni-P-SiO$_2$@Ni composite coating. The results show that the existence of SiO$_2$@Ni nanoparticles can significantly reduce the agglomeration of nanoparticles in the coating. Compared with Ni-P and Ni-P-SiO$_2$ nanocomposite coatings, the Ni-P-SiO$_2$@Ni composite coating exhibits improved corrosion and wear resistance and hydrogen barrier performance. In addition, the Ni-P-SiO$_2$@Ni composite coating also has excellent mechanical properties, with a hardness of up to 340 HV and a bond strength of 15.8 MPa, presenting highly potential industrial applications. This work provides a novel design of protective coating with excellent anti-corrosion resistance and mechanical properties, which has a promising prospect in the development of anti-corrosion coatings for aluminum alloys.

INTRODUCTION

Chemical deposition refers to the process of chemical deposition of metal or alloy from its compound aqueous solution, non-aqueous solution, or molten salt.[1,2] Due to the advantages of simple operation and low cost, chemical deposition has been widely used in various industrial sectors.[3] Among such many chemically deposited coatings, a Ni-P alloy coating with excellent mechanical properties and corrosion resistance is one of the most widely applied coatings. Most recently, Ni-P amorphous alloy coatings were also found to have very low hydrogen diffusivity ($\sim 10^{-14}$ m^2/s) and a good hydrogen barrier property in comparison to low- and medium-carbon steels.[4] Samanta et al.[5] found that a Ni-P amorphous alloy coating displays a slower and delayed H-permeation compared with a crystalline Ni-P alloy coating electroplated on steel at similar coating thickness. In order to further improve the structure and to enhance the wear and corrosion resistance, nanoparticles have been introduced into Ni-P coatings.[6–12] Compared with the traditional Ni-P coating, due to the obviously different microstructure of the Ni-P nanocomposite coating, its mechanical properties and corrosion resistance have been significantly improved. For example, Li et al.[13] introduced Ti nanoparticles into the plating solution to produce a Ni-P-Ti composite coating in order to improve the toughness of Ni-P coatings. Also, the corrosion resistance of Ni-P-Al$_2$O$_3$, Ni-P-SiC, and Ni-P-SiO$_2$ composite coatings[14,15] was found to be much higher than that of traditional Ni-P alloy coatings.

It is well known that the surface of nanoparticles with a number of unsaturated chemical bonds and dangling bonds always has a high surface energy and strong chemical activity, so the agglomeration of nanoparticles is inevitable.[16] Although nanocomposite coatings have shown enhanced properties, it is necessary to overcome the agglomeration of nanoparticles in the preparation process in order to make them play a positive role. Mechanical stirring, ultrasonic dispersion, and adding a

surfactant are conventional methods to overcome the agglomeration.[17] However, the nanoparticles will reunite after being dispersed. Therefore, other more effective methods need to be developed.

The core–shell technology is to coat nanoparticles (such as SiC, SiO_2, etc.) with other atoms in a specific material structure, so that the nanoparticles can form a core–shell structure to realize the dispersion of the nanoparticles and avoid re-agglomeration of nanoparticles under the confinement of the coating structure. At present, the conventional technology for preparing core–shell structure includes radiation methods, micro-emulsion techniques, supercritical techniques, sonochemical reduction, laser ablation, and chemical vapor deposition. For example, Jiang et al.[18] used a one-pot method to prepare Co@C nanoparticles by catalytic carbonization of mixed plastics at high temperatures. El-Gendy et al.[19] obtained Fe@C, Co@C, and Ni@C nanoparticles by high-pressure chemical vapor deposition. Liu et al.[20] used SiO_2 microspheres as templates and adsorbed Ni^{2+} ions on the SiO_2 surface through electrostatic interactions, following which SiO_2@Ni microspheres with raspberry-like morphology and core–shell structure were successfully synthesized by reduction deposition on the surface of the SiO_2 microspheres. In addition, other research has prepared porous SiO_2@Cu/Ni core–shell nanomaterials by the sol–gel method.[21] However, these methods require high-energy conditions and complex equipment.

In this work, in order to reduce the agglomeration phenomenon of nanoparticles in the process of electroless plating and to improve their dispersion in the coatings, a layer of nickel was used to coat the surface of SiO_2 nanoparticles by a simple pre-plating process to obtain SiO_2@Ni nanoparticles. Then, these nanoparticles were introduced into an electroless plating solution for the electroless plating of a Ni-P nanocomposite coating. The formulae of the plating solution and parameters were optimized, and the mechanical properties, corrosion and wear resistance, and hydrogen permeation resistance of the nanocomposite coating were evaluated. This work is beneficial to the development and application of new high-performance Ni-P composite coatings.

MATERIAL AND METHODS

Preparation of SiO_2@Ni Core–Shell Structure and Nanocomposite Coatings

The SiO_2 nanoparticles with the diameter of ~ 50 nm were purchased from Sinopharm. The SiO_2@Ni nanoparticles were prepared according to the following procedures. Firstly, in order to activate the surface of the SiO_2 nanoparticles, they were dispersed in the surfactant solution (sodium dodecyl sulfate, 2 g/L) under ultrasonic stirring for 30 min, and the obtained suspension was then centrifuged and dried, Secondly, the activated

nanoparticles were transferred to a plating solution for 6 h at 80°C. The formula of the electroless plating solution (pH = 3–4) and operational parameters for the pre-plating of nanoparticles are shown in Table S1 (see online supplemental material). Finally, the Ni pre-plated SiO_2 nanoparticles (labeled SiO_2@Ni) after rinsing and centrifugation were achieved.

2024-T6 Al alloy substrates, with a size of $10 \times 10 \times 5$ mm, were purchased from Tianjin Tiangang Guanye (Tianjin, China). The chemical composition of this alloy (in wt.%) is shown in Table S2 (see online supplemental material). The substrates were ground and polished with 800-, 1200-, and 2000-grit emery papers and polishing suspension. Alkaline cleaning was conducted in NaOH solution (20 g/L) for 15 s at 50–60°C. Finally, the substrates were etched in HNO_3 solution (20 wt.%) for 3 min at room temperature. The treated substrate samples were immediately immersed in the electroless plating solution containing the SiO_2@Ni nanoparticles. The electroless plating of Ni-P-SiO_2@Ni nanocomposite coatings was performed at a fixed temperature (90°C) for 3 h.

A series of concentrations of SiO_2@Ni nanoparticles (0 g/L, 2.4 g/L, 3.6 g/L, 4.8 g/L, and 6 g/L) and SiO_2 nanoparticles (3.6 g/L) were studied to optimize the coating composition. As a reference, a Ni-P coating with the same preparation technology and preparation conditions as two nanocomposite coatings were also prepared. The formula of the electroless plating solution (pH = 3–4) for the pre-plating of the nanocomposite coatings and the Ni-P coating is shown in Table S3 (see online supplemental material). The preparation process of the Ni-P-SiO_2@Ni nanocomposite coating is shown in Fig. 1.

Characterization Method

In order to study the morphology of the as-prepared nanoparticles and nanocomposite coatings, optical microscopy (OM) and scanning electron microscopy (SEM) images of nanoparticles and coatings were achieved by a Zeiss Axio Imager 2 and a JEOL JSM 7500F microscope, respectively. The SEM detector types used to characterize the surface and cross-sectional morphology of coatings were SE (with electron beam voltages of 5 kV) and BSE (with electron beam voltages of 20 kV), respectively. X-ray diffraction (XRD) patterns of the specimens were obtained using an X-ray diffractometer (Philips PW1700) with Cu Kα radiation (1.54 Å) operated at 40 kV and 30 mA. The size of the nanoparticles was measured by a Zeta potential analyzer (ZetaAcoustic ZA500). A Vickers microhardness tester (YZHV-1000P) was utilized to measure the microhardness of coatings with a load of 200 g and a holding time of 10 s. The hardness measurements of each samples were repeated at least five times, and the average value was
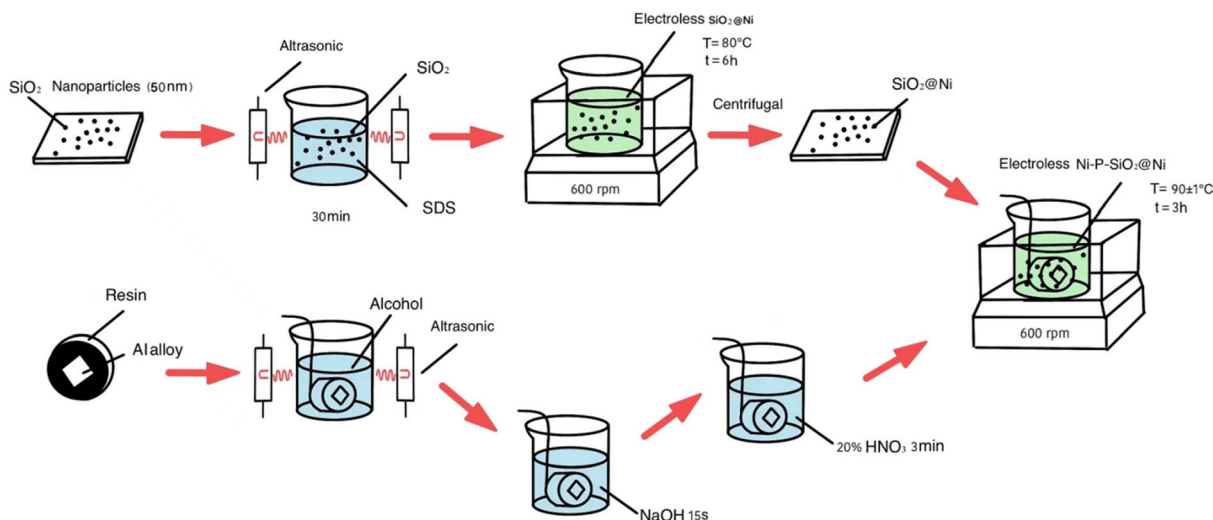
Fig. 1. Preparation scheme of SiO$_2$@Ni nanoparticles and Ni-P-SiO$_2$@Ni nanocomposite coatings by an electroless plating process.

calculated. The bonding strength of the coating on the aluminum alloy substrate was tested according to ASTM D4541, adopting the bonding strength tester (DK-501).

Corrosion and Wear Test

The corrosion performance of the coated samples was evaluated in 3.5 wt.% NaCl solution by measuring the electrochemical impedance spectra (EIS) and potentiodynamic polarization curves. All electrochemical experiments were carried out using a Gamry ESA410 electrochemical workstation. The reference and counter electrodes were saturated calomel electrodes (SCE; + 0.250 V versus SHE) and a platinum sheet with a surface area of 1 cm^2, respectively. All the electrochemical corrosion tests were performed at 25°C under environmental atmosphere. Prior to the EIS tests, the coated sample was immersed in the corrosion solution for 45 min to obtain a steady state at open circuit potential (OCP). The impedance data were collected in the frequency range between 10 MHz and 100 kHz with an excitation amplitude of 10 mV. The analysis of the impedance spectra was performed by fitting the experimental results to equivalent circuits using GamrySoftware_6.32.4217. In addition to the electrochemical experiments, a salt fog test of the coating samples was performed to evaluate the corrosion resistance of the coating. The salt fog test was performed based on ASTM B117.

The wear resistance of the coating was tested by a self-made abrasion experiment device (Fig. S1, see online supplemental material). Before starting the wear test, the front face of the coating sample (i.e., the coating side) was placed onto 1000-grit sandpaper, and the back of the coating sample (i.e., the substrate side) was glued to a glass slide, then a 200-g weight was placed on the glass slide. During the wear test, the glass slide together with the

coating sample was dragged slowly and carefully to realize the abrasion of the coating and the sandpaper. Before and after the wear test within a certain distance (300 cm in this work), the weight loss per unit area (mg/cm^2) of the sample was measured. At the same time, the surface morphology of the worn samples was also observed by SEM.

Electrochemical H-Permeation Test

The electrochemical H-permeation test adopts the Devanathan–Stachurski double electrolytic cell according to the ASTM G-148:2011 standard (Fig. S2, see online supplemental material). The generator cell shown on the right-hand side is a hydrogen-charged generator cell, in which the working electrode (testing sample) and the auxiliary electrode (platinum sheet) are connected to a DC power supply (AN5380-120S). In the charging process of hydrogen to the sample, the testing sample is the cathode where the atomic hydrogen is generated based on the reaction of the H$^+$-obtaining electrons. Part of the atomic hydrogen is recombined into molecular hydrogen and released into the solution and air, but a small amount of atomic hydrogen diffuses into the interior of the sample.

The detector cell shown on the left-hand side is a three-electrode system connected to the electrochemical workstation (Gamry ESA410). The working, reference, and counter electrodes were the testing sample, an SCE (+ 0.250 V versus SHE) and a platinum sheet, respectively. In this detector cell, an oxidation potential, varied from − 1.5 V to + 1.5 V with respect to the OCP was applied to the surface of the testing sample to completely oxidize the H atomic permeating, thereby generating an anodic current, I_a. Accompanied by the hydrogen-charging and hydrogen-oxidizing process of the testing sample, the anode current density gradually increases with time, and finally tends to a
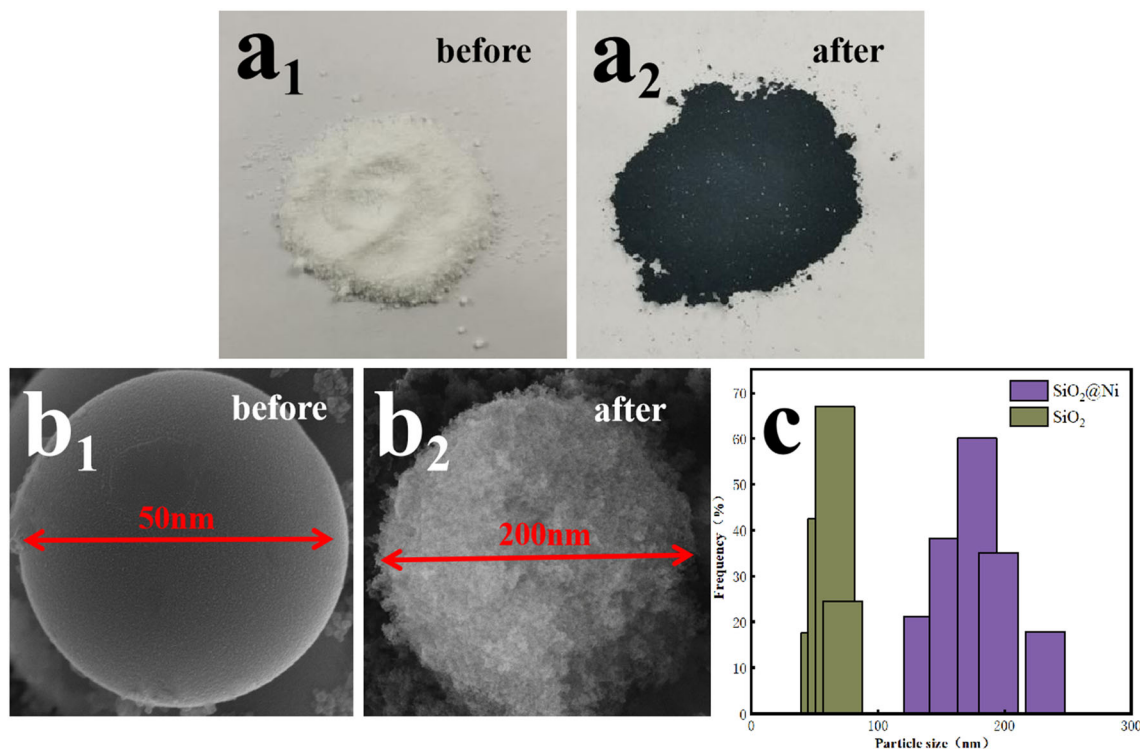
Fig. 2. Macro-morphology of the (a$_1$) SiO$_2$ and (a$_2$) SiO$_2$@Ni nanoparticles, and micromorphology of (b$_1$) SiO$_2$ and (b$_2$) SiO$_2$@Ni nanoparticles; (c) grading curves of the SiO$_2$ and SiO$_2$@Ni nanoparticles.

stable current density value, I_∞, thereby the hydrogen permeation curve is obtained. According to the hydrogen permeation curve, the effective hydrogen diffusion coefficient, D_{eff}, of the coatings can be calculated using the transient time lag method based on:[22,23]

$$D_{eff} = L^2/6t_{0.63} \qquad (1)$$

where L is the thickness of the sample (cm), and $t_{0.63}$ is the time (s) required for the current to reach 0.63 times the stable value of the anode current, I_∞.

RESULTS AND DISCUSSION

Characterization

Characterization of SiO$_2$@Ni Nanoparticles

Figure 2 shows the macro- and micro-morphology of the SiO$_2$ and SiO$_2$@Ni nanoparticles. The color of the SiO$_2$ nanoparticles changes from white to black after electroless plating (Fig. 2a$_1$ and a$_2$), indicating that Ni was plated on their surface, and they are spherical, showing a very smooth surface before plating (Fig. 2b$_1$); however, after plating, the surface of SiO$_2$ nanoparticles becomes rough (Fig. 2b$_2$). As for the size, the diameter of the SiO$_2$@Ni nanoparticles is about 200 nm, which is much larger than that of the original SiO$_2$ nanoparticles ($\sim$ 50 nm). Grading curves illustrate the size distribution of the SiO$_2$ and SiO$_2$@Ni nanoparticles obtained from Zeta potential analysis (Fig. 2c). As

can be seen, the diameter of the SiO$_2$ nanoparticles ranges mostly between 50 nm and 60 nm, while that of the SiO$_2$@Ni particles ranges between 150 nm and 200 nm. The particle size analysis results are consistent with the observation from the SEM images. The size increase of the nanoparticles indicates that the shell of the Ni coating was successfully plated onto the surfaces of the initial SiO$_2$ nanoparticles.[24]

EDS mapping and XRD analysis were carried out to investigate the structure and composition of the nanoparticles after electroless nickel plating, as shown in Fig. 3. The EDS mapping (Fig. 3a) results reveal the presence of the Ni element, indicating the formation of the Ni coating by electroless plating. In the XRD patterns (Fig. 3b), a wide and low peak can be observed at $2\theta = 23°$ in the XRD pattern of the SiO$_2$ nanoparticles, which demonstrates the existence of the nanoparticles in the coating with an amorphous structure.[21] However, there are new crystalline peaks present in the XRD pattern of the SiO$_2$@Ni nanoparticles. The peaks located at 2θ of 44° and 51° can be indexed to the (111) and (200) crystalline planes of face-centered cubic Ni, respectively. The XRD results also confirm the formation of the Ni coating on the surface of the SiO$_2$ nanoparticles. It is worth noting that a small peak is present at 2θ of 40°, which might be attributed to the nickel silicate hydrate (Ni$_3$Si$_2$O$_5$(OH)$_4$)[25] formed through the chemical reaction between Ni^{2+} and SiO$_2$.
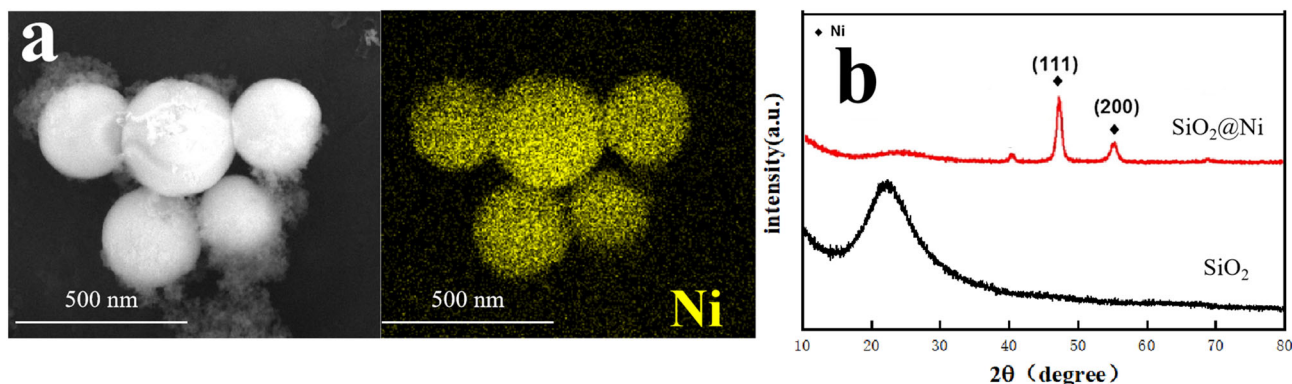
Fig. 3. (a). Element mapping results of SiO$_2$@Ni nanoparticles; (b) XRD patterns of SiO$_2$ and SiO$_2$@Ni nanoparticles.

Characterization of the Nanocomposite Coatings

XRD patterns for the Ni-P, Ni-P-SiO$_2$, and Ni-P-SiO$_2$@Ni coating samples are shown in Fig. 4a, b, and c, respectively. Apart from a diffuse peak at 45° corresponding to the Ni-P amorphous phase, the Ni-P coating has no other obvious diffraction peaks, indicating that the Ni-P coating is completely amorphous. There is no significant difference between the XRD pattern of the Ni-P coating and that of the other two nanocomposite coatings (Ni-P-SiO$_2$@Ni and Ni-P-SiO$_2$). The peaks representing the nanoparticles that appear in Fig. 3b are not detected in the diffraction patterns of the composite coatings shown in Fig. 4b and c, which may be attributed to the low quantity of nanoparticles and the high density of NiP amorphous diffraction peaks.[26] In addition, the absence of new diffraction peaks means that the nanoparticles do not participate in any reaction in the plating process, and so do not affect the amorphous structure of the coating.[27]

The surface morphologies of the as-plated Ni-P, Ni-P-SiO$_2$ and Ni-P-SiO$_2$@Ni nanocomposite coatings are depicted in Fig. 5a, b, and c. The surfaces of the three coatings exhibit a typical cauliflower-like morphology that shows many grains consisted of many fine granules, which is the common feature for the electroless-plated Ni-P based alloys.[28,29] However, compared with the pure Ni-P coating (Fig. 5a$_1$, and a$_2$), the Ni-P-SiO$_2$ nanocomposite coating (Fig. 5b$_1$ and b$_2$) exhibits many bulges which may be attributed to the agglomeration of SiO$_2$ nanoparticles.[30] In contrast, the surface of the Ni-P-SiO$_2$@Ni nanocomposite coating (Fig. 5c$_1$ and c$_2$) with many fewer bulges is smoother than the Ni-P-SiO$_2$ nanocomposite coating. Furthermore, based on the result of EDS mapping performed on the surface of the Ni-P-SiO$_2$@Ni nanocomposite coating (Fig. 5d), the elemental distribution of Si and O was found to be relatively uniform, which also indicates the good dispersion of SiO$_2$@Ni nanoparticles in the coating.

In terms of coating thickness, as shown in Fig. 5a$_3$, b$_3$, and c$_3$, the thickness of the Ni-P coating

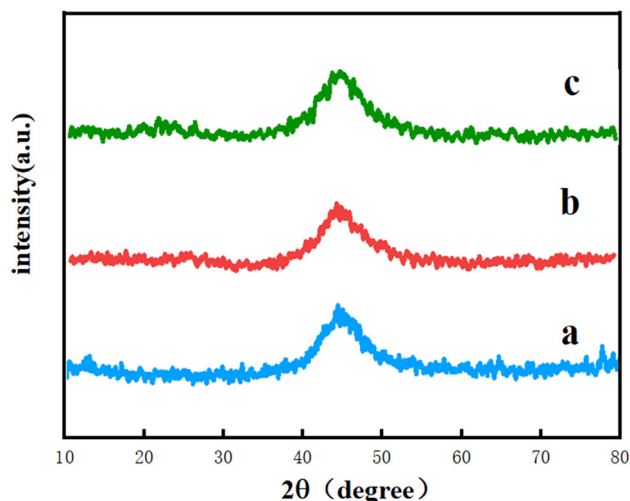Fig. 4. XRD patterns of (a) Ni-P coating, (b) Ni-P-SiO$_2$ (3.6 g/L) coating, and (c) Ni-P-SiO$_2$@Ni (3.6 g/L) coating.

is approximately 15 μm (Fig. 5a$_3$), whereas the SiO$_2$ nanocomposite coatings (Fig. 5b$_3$ and c$_3$) have a thickness of 10–12 μm. This indicates that the existence of the reinforcing phase (SiO$_2$ and SiO$_2$@Ni) in the coating decreases the thickness considerably when the electroless plating conditions are all the same. This is because, when the nanoparticles in the plating solution are adsorbed on the sample surface, the number of catalytic active sites will be reduced and the deposition rate will be reduced.[31] It is worth mentioning that the thickness of the Ni-P-SiO$_2$@Ni composite coating is more uniform than that of the Ni-P-SiO$_2$ coating. This is attributed to the superior dispersion of SiO$_2$@Ni nanoparticles in the plating solution, which provides a more dispersed active site and hence a flatter coating.[32,33]

Mechanical Properties

Hardness and Bonding Strength

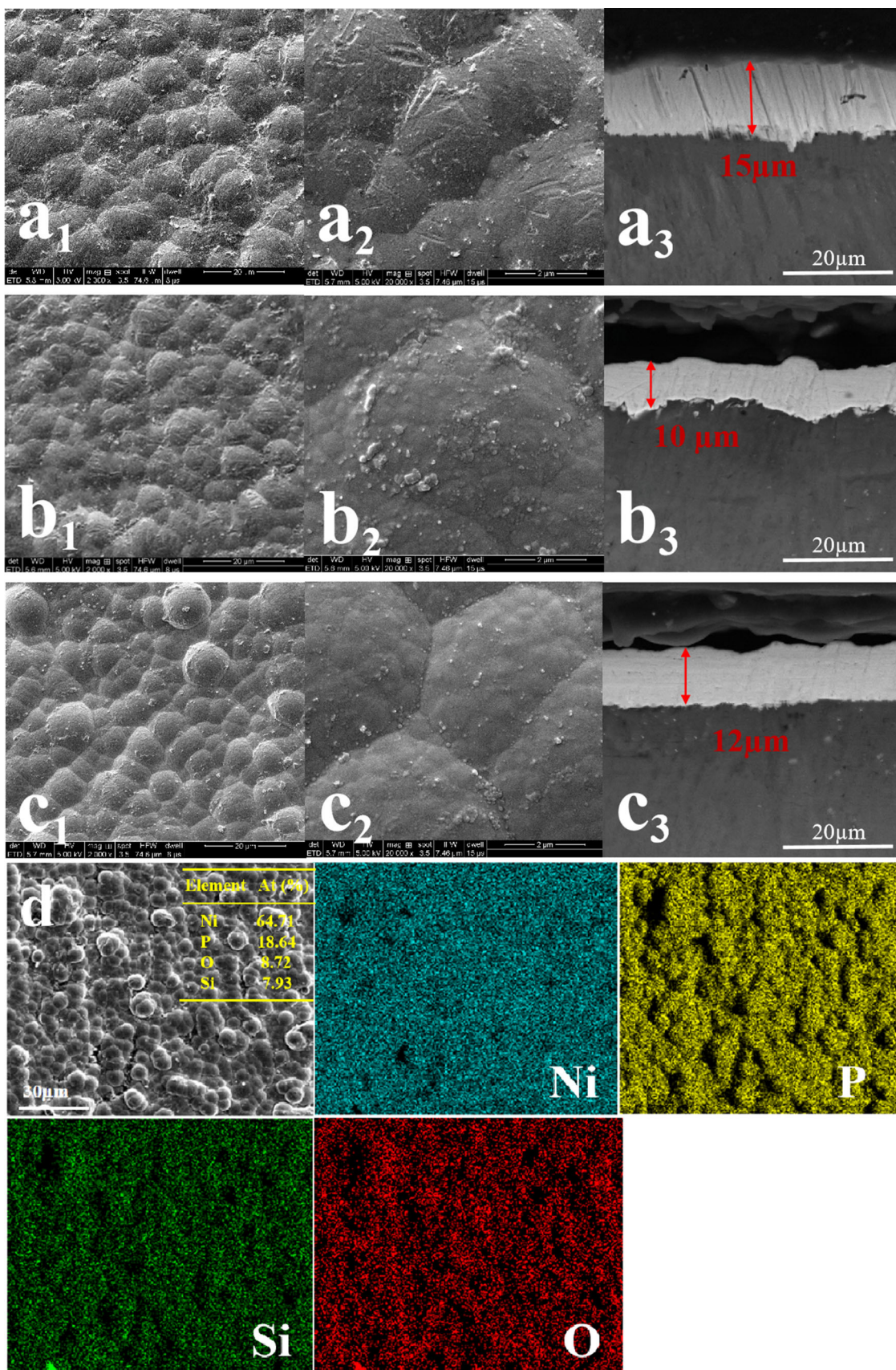Figure 6a shows the effect of the concentration of SiO$_2$@Ni nanoparticles in the plating solution on the

Fig. 5. SEM images of coatings: (a$_1$–a$_3$) Ni-P; (b$_1$–b$_3$) Ni-P-SiO$_2$; (c$_1$–c$_3$) Ni-P-SiO$_2$@Ni; (d) element mapping results of the Ni-P-SiO$_2$@Ni coating.
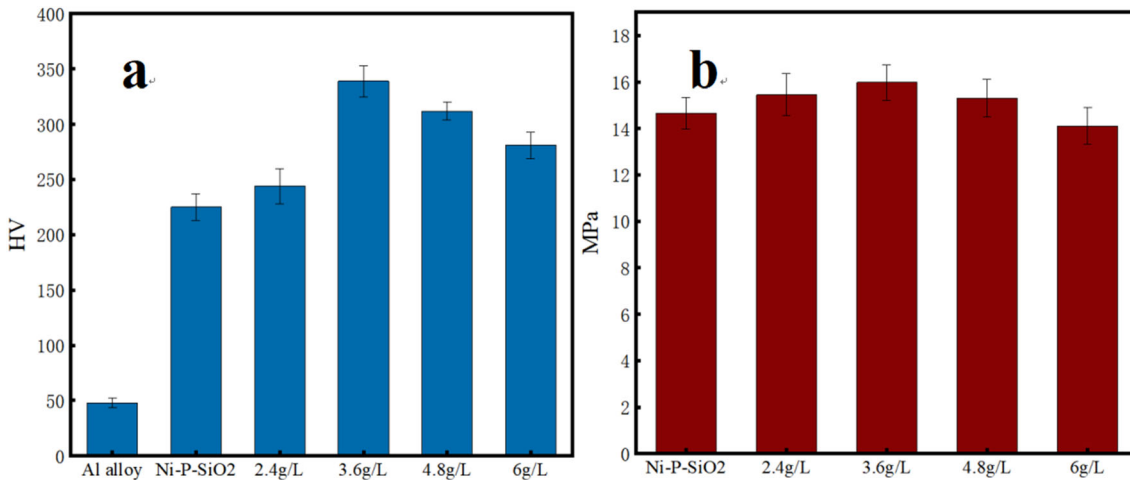
Fig. 6. (a) Vickers hardness and (b) bonding strength of Al alloy, Ni-P-SiO$_2$, and Ni-P-SiO$_2$@Ni coatings prepared with different concentrations of SiO$_2$@Ni nanoparticles in the plating solution.

hardness of the coatings (2.4 g/L SiO$_2$@Ni, 3.6 g/L SiO$_2$, 3.6 g/L SiO$_2$@Ni, 4.8 g/L SiO$_2$@Ni, 6 g/L SiO$_2$@Ni). Generally, compared with the Al alloy and Ni-P-SiO$_2$ nanocomposite coating, the Ni-P-SiO$_2$@Ni nanocomposite coating has a higher hardness. Furthermore, the hardness of Ni-P-SiO$_2$@Ni nanocomposite coating first increases and then decreases with the increase of the concentration of SiO$_2$@Ni nanoparticles. In particular, the Ni-P-SiO$_2$@Ni nanocomposite coating corresponding to the addition of 3.6 g/L SiO$_2$@Ni nanoparticles in the plating solution has the highest hardness of 340 HV. However, when the addition of SiO$_2$@Ni nanoparticles is 6.0 g/L, the hardness of coating drops to 276 HV. In other words, the hardness of Ni-P-SiO$_2$@Ni nanocomposite coating is not completely dependent on the content of dispersed nanoparticles in the plating solution. Figure 6b shows the effect of the concentration of SiO$_2$@Ni nanoparticles in the plating solution on the bonding strength of the coatings. It can be seen that the concentration of SiO$_2$@Ni nanoparticles has the similar but not apparent effect on the bonding strength of the coating as that on the hardness, which is consistent with the cross-section morphology shown in Fig. 5. The bonding strength of the Ni-P-SiO$_2$ coating and Ni-P-SiO$_2$@Ni coatings ranges from 14.2 MPa to 16.1 MPa. The coating corresponding to the concentration of 3.6 g/L-SiO$_2$@Ni nanoparticles in the plating solution has the highest bonding strength of 15.8 MPa. The variation of hardness and bonding strength with the amount of SiO$_2$@Ni nanoparticles can be explained by the inherent characteristic of SiO$_2$ nanoparticles. The elastic modulus of the nanoparticles is different from that of the Ni-P alloy, and the nanoparticles are hard and brittle, therefore the nanoparticles themselves are potential crack sources. Excess nanoparticles will agglomerate and cause more defects in the coating during grain growth. Therefore, controlling the content of

nanoparticles in the composite coating can obtain the coating with the required properties.[34]

Wear Resistance of Coatings

The increase in hardness and bonding strength by adding the SiO$_2$@Ni nanoparticles into the Ni-P coating also improves the wear resistance of the Ni-P-SiO$_2$@Ni nanocomposite coating. Figure 7a shows the weight loss of the Al alloy, Ni-P-SiO$_2$, and Ni-P-SiO$_2$@Ni coatings with the increase of the wear distance. First, the Ni-P based coatings show a much smaller weight loss compared with the Al alloy. The Ni-P-based coatings can be sorted by descending order of weight loss after the same wear distance as Ni-P-SiO$_2$@Ni (6.0 g/L), Ni-P-SiO$_2$@Ni (2.4 g/L), Ni-P-SiO$_2$@Ni (4.8 g/L), and Ni-P-SiO$_2$@Ni (3.6 g/L) coatings. The weight loss of Ni-P-3.6 g/L SiO$_2$@Ni composite coating is the minimum, only 11 mg/cm^2 (the load is 200 g, the sliding distance is 300 cm). Adding nanoparticles to the as-deposited coating decreases the wear weight loss due to an improvement in its hardness, in accordance with previous studies on similar coatings plated on steel substrates.[6,35]

For further analysis, all the worn surfaces were examined by a stereo microscope. As shown in Fig. 7, the surface of the Al alloy is very rough and has deep scratches, and the Ni-P-SiO$_2$@Ni (2.4 g/L, 4.8 g/L, and 6 g/L) coatings exhibit shallower furrows and slight scratches, which can be characterized as slight abrasive and adhesive wear. The surface of the Ni-P-SiO$_2$@Ni (3.6 g/L) coating was very smooth with few scratches, indicating only slight adhesive wear.[36] Due to the high hardness and reinforcement effect of SiO$_2$@Ni nanoparticles on Ni-P coating, the addition of SiO$_2$@Ni nanoparticles also improves the resistance to plastic deformation of the coating. Therefore, the more particles there are, the higher the wear resistance. However, when the SiO$_2$@Ni content is higher than 3.6 g/L in
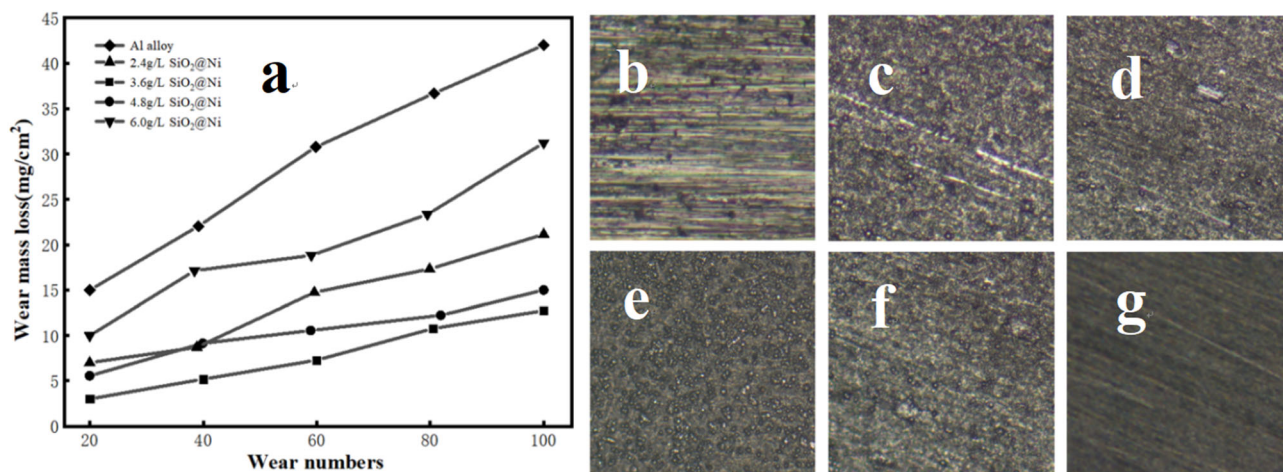
Fig. 7. (a) The relationship between wear mass loss and wear times of Al alloy and coatings; the morphology of the worn surfaces: (b) Al alloy; (c) Ni-P-1.2 g/L SiO₂@Ni; (d) Ni-P-2.4 g/L SiO₂@Ni; (e) Ni-P-3.6 g/L SiO₂@Ni; (f) Ni-P-4.8 g/L SiO₂@Ni; (g) Ni-P-6.0 g/L SiO₂@Ni.3.2 corrosion resistance.

the plating solution, the wear resistance gradually decreases. This might be due to the exfoliation of the nanoparticles, which causes abrasive wear in the process of wear.[37]

Corrosion Resistance

The potentiodynamic polarization curves and the EIS spectra for the Al alloy, Ni-P, Ni-P-SiO₂ (3.6 g/L), and Ni-P-SiO₂@Ni (2.4 g/L, 3.6 g/L, 4.8 g/L, and 6.0 g/L, respectively) coatings in 3.5 wt.% NaCl solution at room temperature are shown in Fig. 8. The equivalent circuits of the measured EIS spectra for both the Ni-P and Ni-P-SiO₂@Ni (SiO₂) coatings are shown in Fig. 8d. The circuit includes the solution resistance (R_s), the polarization resistance (R_p), a Warburg diffusion element (W), and constant phase element: CPE_{dl} for the metal/solution interfaces. The electrochemical parameters (corrosion potential (E_{corr}), corrosion current density (i_{corr}), R_s, R_p) derived from fitting the measured data using the equivalent circuits are listed in Table S4 (see online supplemental material).

It can be seen from Table S4 and Fig. 8a that the E_{corr} and i_{corr} of the Ni-P coating are − 298 mV and 78.2 μA/cm², respectively. Compared with the Ni-P coating, the i_{corr} and E_{corr} of the Ni-P-SiO₂@Ni coatings decrease and positively shift, respectively, indicating that the corrosion rate of the coatings is significantly reduced and the corrosion resistance of the coatings is improved. However, when excessive SiO₂@Ni is added to the plating solution, the E_{corr} of the composite coating has a negative shift, and the i_{corr} decreases, thus the corrosion resistance of the coating decreases. This is because the existence of the SiO₂@Ni significantly reduces the agglomeration phenomenon of SiO₂, and the various defects caused by the agglomeration phenomenon are also greatly reduced, so that the strengthening effect of the particles on the coating is increased[38] and the

corrosion resistance is enhanced. On the other hand, co-deposited nanoparticles act as barriers to the invading corrosive media.[24] Accordingly, the incorporation of SiO₂@Ni changes the alloy microstructure and stops corrosion paths proceeding, which finally results in a higher corrosion resistance of the Ni-P-SiO₂@Ni composite coating with respect to the Ni-P coating.[39] The improved corrosion resistance of the Ni-P-SiO₂@Ni composite coating is also confirmed by the impedance curve. As shown in Fig. 8b and c and Table S4, the coating is highly protective when it has a high impedance |Z| at low frequencies, i.e., high polarization resistance (R_p) and low capacitances. The R_p value (10,024–47,721 Ω cm²) at the low frequency of the Ni-P-SiO₂@Ni (2.4–4.8 g/L) coatings is significantly higher than that of the other coatings. However, the R_p for the Ni-P-SiO₂@Ni coatings is decreased from 47,721 Ω cm² to 6107 Ω cm² when the SiO₂@Ni concentration in the plating solution increases from 3.6 g/L to 6 g/L. This is the same as the result of the potentiodynamic polarization curves.

Figure 9 shows the corrosion morphology of the Ni-P-SiO₂ and Ni-P-SiO₂@ Ni coatings after a 96-h salt spray test. It can be clearly seen that the Ni-P-SiO₂@Ni coating is slightly corroded, and that the corrosion mainly occurs at the grain boundary, while the Ni-P-SiO₂ coating suffers more severe corrosion not only at the grain boundary but the grains have also been severely corroded.[5] These test results are consistent with the results obtained from the polarization curves.

Hydrogen Permeation Resistance

Hydrogen permeation curves for the Al alloy and different Ni-P-based coatings are shown in Fig. 10. The anodic current of the coatings with the time change trend is the same. At the initial stage of the test, the hydrogen-charged side (coating) was
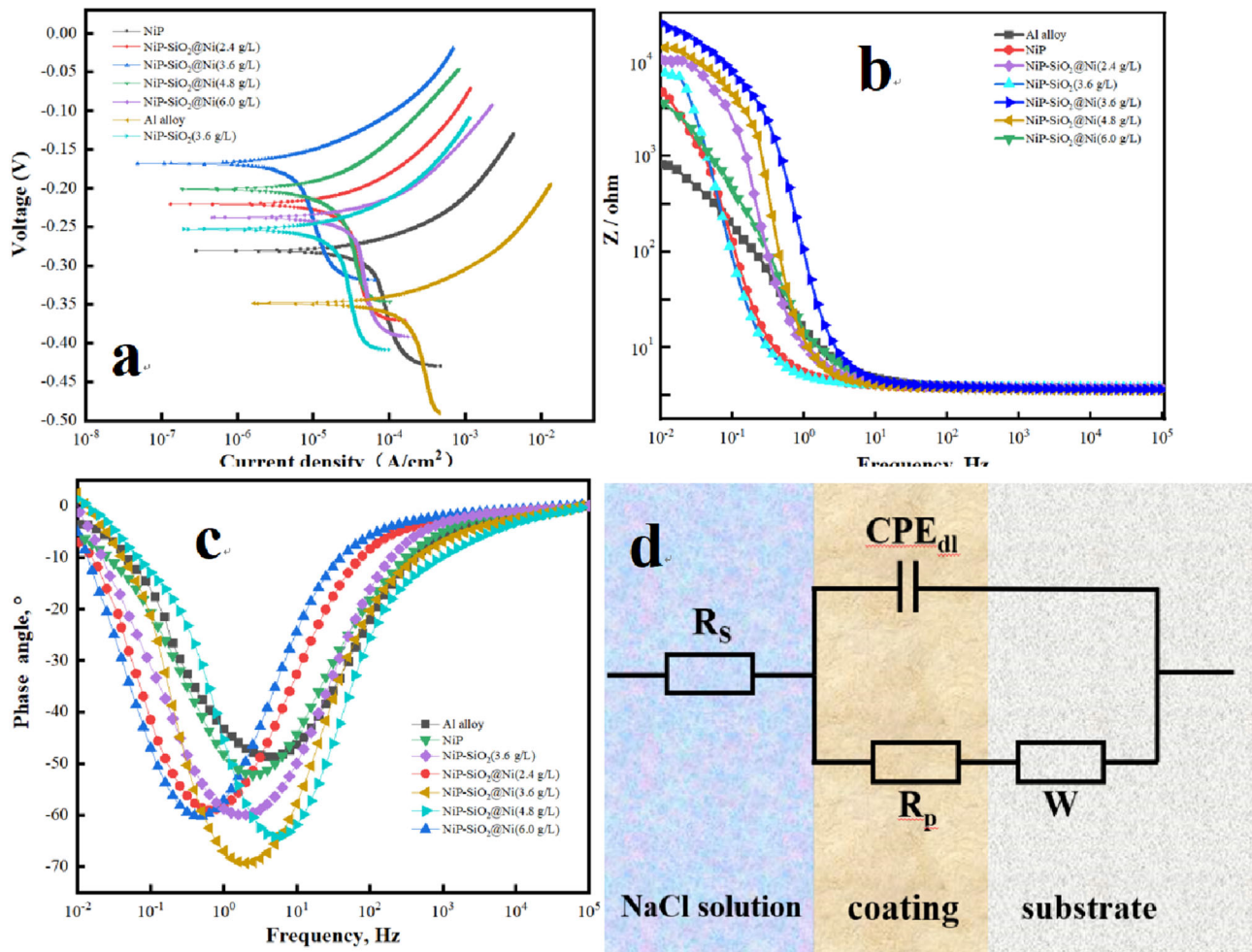
Fig. 8. (a) Polarization curves, (b) Bode and (c) corresponding phase angle plots of the substrate, and coatings in a 3.5 wt.% NaCl solution at room temperature; (d) equivalent electric circuits for coatings in 3.5 wt.% NaCl solution.

producing H atoms entering from the coating surface. However, it has not yet diffused to the hydrogen expansion side of the electrolytic cell, so the anodic currents are all 0 μA. After a period of time, the anodic current begins to increase with time, i.e., H atoms diffuse to the anode (bare steel) on the hydrogen-expanding side and ionize to form H^+, which moves directionally at a constant potential to form the anodic current, I_a. Finally, as the number of H atoms arriving at the anode increases, I_a gradually increases and tends to a stable value, I_∞, after penetrating the coating.

Overall, a huge steady-state H permeation current can be observed in the case of the uncoated Al alloy substrates. However, when the substrate is plated with a Ni-P-based coating by electroless plating, a lower H permeation current is observed. The H permeation is further reduced in the case of the Al alloy plated with the Ni-P-SiO$_2$@Ni coating. On the electrochemical workstation side, the coating thicknesses of the Ni-P-SiO$_2$@Ni coatings (2.4 g/L, 3.6 g/L, 4.8 g/L, and 6.0 g/L) were almost maintained at ~ 12 μm. Even so, the best hydrogen

barrier performance of the coating was achieved when the nanoparticle content in the plating solution was 3.6 g/L. According to Eq. 1, the effective hydrogen diffusion coefficient (D_{eff}) can be calculated, as shown in Table I. With the increase of the SiO$_2$@Ni nanoparticle concentration, D_{eff} first decreases and then increases. When the concentration of SiO$_2$@Ni reaches 3.6 g/L, its effective hydrogen diffusion coefficient, D_{eff}, reaches a minimum of 4.02×10^{-7} cm^2/s, and the hydrogen barrier performance is the best. The uniform, hard and compact coating of the amorphous Ni-P layer formed by an electroless process shows good resistance to hydrogen permeation. When the nanoparticles are dispersed in the coating, the permeability path of the hydrogen atoms can be prolonged, thus significantly improving the hydrogen permeation resistance of the coating. In contrast, excess nanoparticles will aggregate in the coating, increasing its defects, and hydrogen atoms will spread along the defects, resulting in decreased hydrogen permeation resistance.
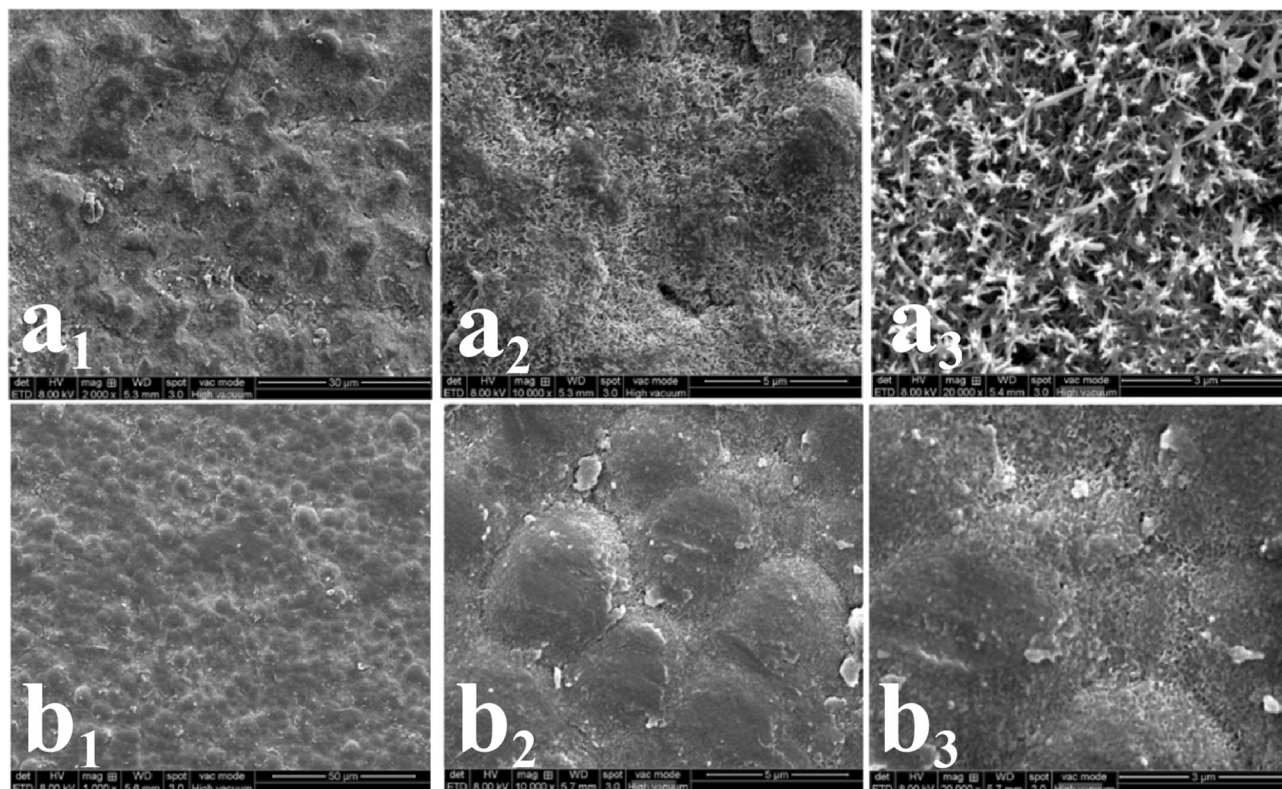
Fig. 9. The micro-morphology of the coatings after corrosion: (a₁–a₃) Ni-P-SiO₂@Ni; (b₁–b₃) Ni-P-SiO₂.
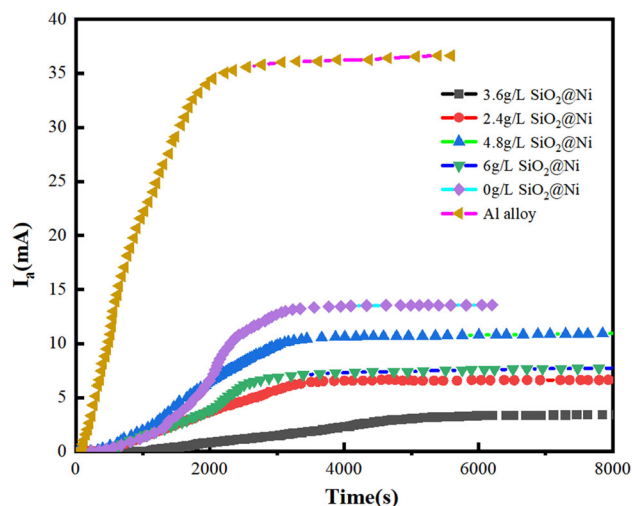

Fig. 10. Hydrogen permeation curves of the Al alloy and different Ni-P composite coatings.

CONCLUSION

Aiming to reduce the agglomeration of nanoparticles in the coatings, core–shell SiO_2@Ni nanoparticles were prepared by electroless plating. Pre-plating of nanoparticles can effectively reduce their high surface energy so as to reduce agglomeration and make them uniformly dispersed in the coatings. Ni-P, Ni-P-SiO_2, and Ni-P-SiO_2@Ni coatings with different contents of pre-plated nanoparticles were prepared by electroless plating. Through SEM and XRD characterization, the microstructure and mechanical properties of the coatings were studied, and it was found that the Ni-P-SiO_2@Ni coating has the smallest grains and the most uniform distribution of nanoparticles. Through the hardness test, we found that, when the content of SiO_2@Ni nanoparticles reaches 3.6 g/L in the plating solution, the hardness of the coating is the largest (340 HV).

In the corrosion resistance test, the electrochemical test and the salt fog testing have proved that the corrosion resistance of the Ni-P-SiO_2@Ni composite coating is better than that of the other coatings. When the content of SiO_2@Ni nanoparticles reaches 3.6 g/L, the corrosion resistance of the coating is the best. The wear test also reflects that the wear resistance of the Ni-P-3.6 g/L SiO_2@Ni composite coating is the best of all the coatings. Therefore, in the Ni-P-SiO_2@Ni coating system, 3.6 g/L-SiO_2@Ni is the optimal content.

This has been proven again by the H-permeation test, In the electrochemical hydrogen permeation experiment, it was found that the Ni-P nanocomposite coating has excellent hydrogen permeation barrier properties, based on its amorphous structure and the strengthening effect of the nanoparticles. In terms of the hydrogen barrier, when the concentration of nanoparticles reaches 3.6 g/L, the enhancement effect is the best, which corresponds to other properties of the coating. The preparation of core–shell-structured nanoparticles greatly

Table I. Effective hydrogen diffusion coefficient of Al alloy and Ni-P composite coatings

Concentration of SiO$_2$@Ni (g/L)	L (mm)	I_∞ (μA)	$t_{0.63}$ (s)	D_{eff} (10^{-7} cm^2/s)
0	1.00	13.48	2750	6.06
2.4	1.00	7.22	3130	5.32
3.6	1.00	3.67	4250	3.92
4.8	1.00	6.85	3000	5.56
6.0	1.00	10.18	2910	5.72
Al alloy	1.00	36.75	1560	10.68

improves the corrosion resistance, wear resistance, and hydrogen barrier properties of ordinary nanocomposite coatings, and the preparation process is efficient, which has great research value.

SUPPLEMENTARY INFORMATION

The online version contains supplementary material available at https://doi.org/10.1007/s11837-024-06457-x.

CONFLICT OF INTEREST

We declare that we have no financial and personal relationships with other people or organizations that can inappropriately influence our work, there is no professional or other personal interest of any nature or kind in any product, service and/or company that could be construed as influencing the position presented in or the review of the manuscript entitled "Novel nano core-shell structure SiO$_2$@Ni reinforced Ni-P based amorphous composite coating".

REFERENCES

1. M. Palaniappa and S.K. Seshadri, *Mater. Sci. Eng. A* 460–461, 638 https://doi.org/10.1016/j.msea.2007.01.134 (2007).
2. P. Sahoo and S.K. Das, *Mater. Des.* 32, 1760 https://doi.org/10.1016/j.matdes.2010.11.013 (2011).
3. L. Benea, P.L. Bonora, A. Borello, and S. Martelli, *Mater. Corros.* 53, 23 https://doi.org/10.1002/1521-4176(200201)53:1 (2002).
4. H.K.D.H. Bhadeshia, *ISIJ Int.* 56, 24 https://doi.org/10.2355/isijinternational.ISIJINT-2015-430 (2016).
5. S. Samanta, C. Singh, A. Banerjee, K. Mondal, M. Dutta, and S.B. Singh, *Surf. Coat. Technol.* 403, 126356 https://doi.org/10.1016/j.surfcoat.2020.126356 (2020).
6. C.K. Chen, H.M. Feng, H.C. Lin, and M.H. Hon, *Thin Solid Films* 416, 31 https://doi.org/10.1016/S0040-6090(02)00628-4 (2002).
7. L. Shi, C. Sun, P. Gao, F. Zhou, and W. Liu, *Appl. Surf. Sci.* 252, 3591 https://doi.org/10.1016/j.apsusc.2005.05.035 (2006).
8. P.A. Gay, P. Bercot, and J. Pagetti, *Surf. Coat. Technol.* 140, 147 https://doi.org/10.1016/S0257-8972(01)01043-X (2001).
9. Y.Y. Liu, J. Yu, H. Huang, B.H. Xu, X.L. Liu, Y. Gao, and X.L. Dong, *Surf. Coat. Technol.* 201, 7246 https://doi.org/10.1016/j.surfcoat.2007.01.035 (2007).
10. M. Rezrazi, M.L. Doche, P. Berçot, and J.Y. Hihn, *Surf. Coat. Technol.* 192, 124 https://doi.org/10.1016/j.surfcoat.2004.04.067 (2005).
11. V.S. Protsenko, D.A. Bogdanov, S.A. Korniy, A.A. Kityk, A.S. Baskevich, and F.I. Danilov, *Int. J. Hydrog. Energy* 44, 24604 https://doi.org/10.1016/j.ijhydene.2019.07.188 (2019).
12. G. Vidrich, J.F. Castagnet, and H. Ferkel, *Electrochem. Soc.* 152, C294 https://doi.org/10.1149/1.1885286 (2005).
13. Z. Li, Z. Farhat, G. Jarjoura, E. Fayyad, A. Abdullah, and M. Hassan, *Tribol. Trans.* 62, 880 https://doi.org/10.1080/10402004.2019.1634227 (2019).
14. S. Karthikeyan and B. Ramamoorthy, *Appl. Surf. Sci.* 307, 654 https://doi.org/10.1016/j.apsusc.2014.04.092 (2014).
15. H. Ashassi-Sorkhabi and M. Es'haghi, *Corros. Sci.* 77, 185 https://doi.org/10.1016/j.corsci.2013.07.046 (2013).
16. D. Dong, X.H. Chen, W.T. Xiao, G.B. Yang, and P.Y. Zhang, *Appl. Surf. Sci.* 255, 7051 https://doi.org/10.1016/j.apsusc.2009.03.039 (2009).
17. H.-Y. Zheng, M.-Z. An, and J.-F. Lu, *Appl. Surf. Sci.* 254, 1644 https://doi.org/10.1016/j.apsusc.2007.07.110 (2008).
18. J. Gong, J. Liu, X. Chen, Z. Jiang, X. Wen, E. Mijowska, and T. Tang, *J. Mater. Chem. A* 2, 7461 https://doi.org/10.1039/c4ta00173g (2014).
19. A.A. El-Gendy, E.M.M. Ibrahim, V.O. Khavrus, Y. Krupskaya, S. Hampel, A. Leonhardt, B. Büchner, and R. Klingeler, *Carbon* 47, 2821 https://doi.org/10.1016/j.carbon.2009.06.025 (2009).
20. X. Liu, Y. Liu, X. Shi, Z. Yu, and L. Feng, *Appl. Phys. A* 122, 987 https://doi.org/10.1007/s00339-016-0526-5 (2016).
21. L. Wang, N. Zuo, Q. Liu, D. Xie, S. Meng, N. Mominou, Y. Ma, and C. Jing, *J. Alloys Compd.* 855, 157516 https://doi.org/10.1016/j.jallcom.2020.157516 (2021).
22. Y. Wang, D. Liu, S. Feng, Y. Zhang, T. Ouyang, and J. Suo, *Surf. Coat. Technol.* 307, 271 https://doi.org/10.1016/j.surfcoat.2016.08.082 (2016).
23. M. Tamura and T. Eguchi, *J. Vac. Sci. Technol. A Vac. Surf. Films* 33, 041503 https://doi.org/10.1116/1.4919736 (2015).
24. P. Sun, Z. Dong, Y. Chen, H. Yan, C. Luo, H. Song, and Z. Hu, *Appl. Surf. Sci.* 526, 146660 https://doi.org/10.1016/j.apsusc.2020.146660 (2020).
25. J. Pu, Q.W. Chen, L.Q. Hao, R.F. Tian, L.X. Zhang, and L. Wang, *J. Phys. Chem. B* 108, 6311 https://doi.org/10.1021/jp049754g (2004).
26. E. Fayyad, A. Abdullah, M. Hassan, A. Mohamed, C. Wang, G. Jarjoura, and Z. Farhat, *Coatings* 8, 37 https://doi.org/10.3390/coatings8010037 (2018).

27. J.N. Balaraju, V. Ezhil Selvi, and K.S. Rajam, *Mater. Chem. Phys.* 120, 546 https://doi.org/10.1016/j.matchemphys.2009.11.047 (2010).

28. S. Sadreddini and A. Afshar, *Appl. Surf. Sci.* 303, 125 https://doi.org/10.1016/j.apsusc.2014.02.109 (2014).

29. S. Afroukhteh, C. Dehghanian, and M. Emamy, *Prog. Nat. Sci. Mater. Int.* 22, 318 https://doi.org/10.1016/j.pnsc.2012.06.006 (2012).

30. M. Sarret, C. Müller, and A. Amell, *Surf. Coat. Technol.* 201, 389 https://doi.org/10.1016/j.surfcoat.2005.11.127 (2006).

31. C.J. Lin, K.C. Chen, and J.L. He, *Wear* 261, 1390 https://doi.org/10.1016/j.wear.2006.03.054 (2006).

32. F. Bigdeli and S.R. Allahkaram, *Mater. Des.* 30, 4450 https://doi.org/10.1016/j.matdes.2009.04.020 (2009).

33. M. Habibnejad-Korayem, R. Mahmudi, H.M. Ghasemi, and W.J. Poole, *Wear* 268, 405 https://doi.org/10.1016/j.wear.2009.08.031 (2010).

34. N. Ghavidel, S.R. Allahkaram, R. Naderi, M. Barzegar, and H. Bakhshandeh, *Surf. Coat. Technol.* 382, 125156 https://doi.org/10.1016/j.surfcoat.2019.125156 (2020).

35. C.A. León-Patiño, J. García-Guerra, and E.A. Aguilar-Reyes, *Wear* 426–427, 330 https://doi.org/10.1016/j.wear.2019.02.015 (2019).

36. L. Yu, W. Huang, and X. Zhao, *J. Alloys Compd.* 509, 4154 https://doi.org/10.1016/j.jallcom.2011.01.025 (2011).

37. S. Zhang, K. Han, and L. Cheng, *Surf. Coat. Technol.* 202, 2807 https://doi.org/10.1016/j.surfcoat.2007.10.015 (2008).

38. I.R. Mafi and C. Dehghanian, *Appl. Surf. Sci.* 258, 1876 https://doi.org/10.1016/j.apsusc.2011.10.095 (2011).

39. J. Hu, L. Fang, X.L. Liao, and L.T. Shi, *Surf. Eng.* 33, 362 https://doi.org/10.1080/02670844.2016.1230975 (2016).